Open access • Journal Article • DOI:10.1103/PHYSREVB.90.165420

Tuning photoinduced terahertz conductivity in monolayer graphene: Optical-pump terahertz-probe spectroscopy — Source link

Srabani Kar, Dipti R. Mohapatra, Eric Freysz, A. K. Sood

Institutions: Indian Institute of Science, University of Bordeaux

Published on: 16 Oct 2014 - Physical Review B (AMER PHYSICAL SOC)

Topics: Graphene, Fermi energy and Terahertz radiation

Tuning photoinduced terahertz conductivity in monolayer graphene: Optical-pump terahertz-probe spectroscopy

Srabani Kar,[1,2] Dipti R. Mohapatra,[1] Eric Freysz,[3] and A. K. Sood[1,2,*]
[1]*Department of Physics, Indian Institute of Science, Bangalore 560 012, India*
[2]*Center for Ultrafast Laser Applications, Indian Institute of Science, Bangalore 560 012, India*
[3]*University of Bordeaux, LOMA, UMR CNRS 5798, 351, Cours de la liberation, 33405 Talence cedex, France*
(Received 11 June 2014; revised manuscript received 16 August 2014; published 16 October 2014)

Optical-pump terahertz-probe differential transmission measurements of as-prepared single layer graphene (AG) (unintentionally hole doped with Fermi energy E_F at ~ -180 meV), nitrogen doping compensated graphene (NDG) with $E_F \sim -10$ meV, and thermally annealed doped graphene (TAG) are examined quantitatively to understand the opposite signs of photoinduced dynamic terahertz conductivity $\Delta\sigma$. It is negative for AG and TAG but positive for NDG. We show that the recently proposed mechanism of multiple generations of secondary hot carriers due to Coulomb interaction of photoexcited carriers with the existing carriers together with the intraband scattering can explain the change of photoinduced conductivity sign and its magnitude. We give a quantitative estimate of $\Delta\sigma$ in terms of controlling parameters—the Fermi energy E_F and momentum relaxation time τ. Furthermore, the cooling of photoexcited carriers is analyzed using a supercollision model which involves a defect mediated collision of the hot carriers with the acoustic phonons, thus giving an estimate of the deformation potential.

DOI: 10.1103/PhysRevB.90.165420 PACS number(s): 81.05.ue, 78.47.−p, 78.20.Ci, 78.67.Wj

I. INTRODUCTION

The performance of electronic and optoelectronic devices depends on the material properties such as carrier mobility, energy conversion efficiency from photon to electron-hole pairs, spectral response, and equilibration of the photogenerated carriers. The linear band dispersion with zero band gap in monolayer graphene responsible for many fascinating transport phenomena and optical effects makes graphene a desirable material for high speed optoelectronic devices [1–7]. A key question to answer in optoelectronic applications is the relaxation of the hot carriers in conical energy-momentum space of the monolayer graphene. Ultrafast time resolved pump-probe spectroscopy [8–12] and angle resolved photoemission spectroscopy [13] have been shown to be excellent probes of nonequilibrium carrier dynamics in graphene. The terahertz-probe pulse following the optical pump examines the intraband scattering dynamics as compared to optical probe which is sensitive to both interband and intraband scattering processes. Following the pump pulse, the photoexcited carriers achieve a quasiequilibrium Fermi-Dirac distribution, characterized by electron temperature T_e, mostly by carrier-carrier scattering. The cooling of the carriers can occur through phonon emission as well as through carrier-carrier scattering. The latter involves the transfer of energy of photoexcited carriers to the existing carriers in graphene (making them hot) [14–16]. The cooling via phonon emission involving optical phonons occurs on a time scale of ∼100 to 500 fs till the energy of the photoexcited carriers is less than the optical phonon energy (∼200 meV). This is followed by the direct coupling between the carriers and acoustic phonons which can last for tens of picoseconds. However, the carrier-acoustic phonon relaxation time is reduced to less than 10 ps when large momentum and large energy acoustic phonons emission occurs mediated by the disorder. This three body (carriers + acoustic phonons + disorder) mediated cooling is termed as supercollision cooling of the carriers [17]. Several groups have reported optical-pump terahertz-probe (OPTP) time domain spectroscopy of epitaxial grown as well as CVD grown graphene showing positive [9,10,18,19] as well as negative dynamic conductivity [16,20–22]. The positive dynamic conductivity can be easily understood in terms of intraband scattering of the carriers. Docherty *et al.* [20] showed that the THz photoconductivity changes from positive in vacuum to negative in nitrogen, air, and oxygen environment and proposed stimulated THz emission from photoexcited graphene as the cause of the negative photoconductivity. Several other experimental [23] and theoretical [24,25] studies have also attributed the negative dynamic conductivity to the amplified stimulated terahertz emission above a threshold pump intensity [26]. In this context, Gierz *et al.* [13] have shown experimentally that only within 130 fs after photoexcitation, the Fermi-Dirac distribution for electron and holes are different, suggesting that population inversion and hence stimulated emission is not feasible beyond this time window. Jnawali *et al.* [21] have attributed the decrease in photoconductivity to the increase in carrier scattering rate with negligible increase of Drude weight. Tielrooij *et al.* [16] have proposed to explain the negative dynamic conductivity via Coulomb interaction governed carrier-carrier scattering where the energy of the photoexcited carriers is transferred to the existing carriers in the Dirac cone, a process termed as secondary hot carrier generation (SHCG). In a very recent study of tuning the sign of OPTP signal from the single layer graphene (SLG) using electrostatic top gating, [27] the explanation given is as follows: Taking conductivity $\sigma = \mathfrak{D}/\Gamma$, the dynamic conductivity $\Delta\sigma = (\Delta\mathfrak{D}/\mathfrak{D}_0)\sigma_0 - (\Delta\Gamma/\Gamma_0)\sigma_0$, where $\mathfrak{D}$ is the Drude weight, Γ is the carrier scattering rate, and the subscript 0 stands for the pump off condition. The contribution from the Drude weight dominates near the charge neutral point and is positive. For higher doping, the contribution from

*Corresponding author: asood@physics.iisc.ernet.in

change of scattering rate $\Delta\sigma_\Gamma = -(\Delta\Gamma/\Gamma_0)\sigma_0$ controls the $\Delta\sigma$. The authors [27] assumed $\Delta\Gamma/\Gamma_0 = 0.2$, independent of E_F, to explain the negative dynamic conductivity. This framework does not explain the observed saturation behavior of the dynamic conductivity at higher Fermi energy. Therefore, the issue of the optical-pump induced terahertz conductivity, in particular its sign and amplitude, is still open and needs to be understood quantitatively.

In this work we report the THz conductivity $\sigma(\omega)$ of (1) as-grown single layer graphene (AG) by chemical vapor deposition which is unintentionally hole doped, (2) nitrogen doping compensated monolayer graphene (NDG), and (3) thermally annealed nitrogen doped graphene (TAG). The samples have different values of carrier momentum relaxation time τ and the Fermi energy E_F. The conductivities obtained from the THz transmission measurements compare well with the estimates from the relative Raman intensities of D and G bands. Next, we present optical pump (1.58 eV) THz probe measurements of the transient THz photoconductive response of the graphene samples. On photoexcitation, the dynamic conductivity [$\Delta\sigma = \sigma(\text{pump on}) - \sigma(\text{pump off})$] is negative for the AG but positive for the NDG. In both cases, the $|\Delta\sigma|^{\max}$ is $\sim 1.5G_0$, where $G_0 = 2e^2/h (= 77.3\mu S)$ is quantum of conductance. We show that on thermal annealing the NDG, the $\Delta\sigma$ is once again negative. A quantitative analysis of $\Delta\sigma$ is done by noting that in the terahertz range, intraband scattering contribution to $\Delta\sigma$ is orders of magnitude larger than the interband contribution. We invoke secondary hot carrier generation (SHCG) [16] to explain quantitatively the negative $\Delta\sigma$ in AG. The sign and magnitude of the dynamic conductivity in graphene thus depends on the relative contributions of the intraband scattering and the SHCG, which, in turn, depend on the momentum relaxation time and the Fermi energy. The cooling of hot carriers is quantitatively analyzed in terms of supercollision (SC) processes. The frequency dependence of dynamic conductivity is also measured and analyzed in terms of the Drude-Lorentz model.

II. METHOD

A. Terahertz setup

The output beam of the Ti:sapphire regenerative amplifier laser system which produces ~50 fs optical pulses at a central wavelength of 785 nm with a repetition rate of 1 kHz is divided into three parts: for terahertz generation, terahertz detection, and optical pumping. The terahertz radiation is generated by co-focusing the fundamental and its second harmonic beam using a 10 cm focal length lens to produce plasma in air. The unwanted light following the plasma was blocked using a high resistive silicon wafer. The terahertz was collimated and focused on the sample by a pair of off-axis parabolic mirrors and again collimated and focused by parabolic mirrors on a 1 mm thick ZnTe crystal used as a detector. All experiments were carried out in transmission geometry in a nitrogen environment at room temperature. The estimated terahertz electric field is ~30 kV/cm. The optical-pump-induced changes in the terahertz transmission were measured at the maximum position of the terahertz electric field. The spot size of the pump beam was ~0.7 cm and the spot size of the terahertz beam was ~0.3 cm so that the pump can excite the sample uniformly. To measure the photoinduced transmission the chopper (341 Hz) was placed in the pump path and to measure the THz electric field from the unexcited sample, the chopper was placed in the path of the terahertz beam.

B. Sample preparation

The graphene samples were grown by using the well-known chemical vapor deposition (CVD) method on 25 μm thick copper foil [28]. Before growth, the copper foils were cleaned through a chemical process using acetone, acetic acid, deionized water, isopropyl alcohol, and methanol successively. In order to remove the oxides and chemical residues, the copper substrates were heated at 1000 °C for 30 min in the presence of hydrogen at a pressure of 20 Torr. Subsequently, methane was flowed into the chamber and graphene growth was carried out for 30 min keeping hydrogen and methane at a fixed ratio of 1:3, followed by stoppage of the methane flow, and the system was allowed to cool at a rate of 20 °C/min for first 20 min without changing the hydrogen flow rate. Then, the system was cooled by a normal fan up to a temperature of 350 °C in 1 h, followed by natural cooling to room temperature. For nitrogen doping, protocol was similar to that reported recently [29]. Namely, after stopping the methane flow and cooling the system to 850 °C, ammonia (10 sccm) was passed for 10 min. Subsequently, ammonia flow was stopped and the system was cooled in a hydrogen atmosphere as described before. Graphene was transferred onto the 1 mm thick α quartz by the PMMA technique [30].

III. RESULTS AND DISCUSSIONS

A. Characterization of the samples

Primarily, the experiments were carried out on two samples: AG and NDG. Later, to check the effect of temperature annealing, the NDG was annealed at 400 °C for 4 h in argon atmosphere and all the experiments were also performed on this thermally annealed graphene (TAG). The x-ray photoemission spectroscopy (XPS) was done to confirm the presence and nature of nitrogen in graphene. The samples were further characterized by Raman spectroscopy at room temperature using $\lambda = 514$ nm of laser light.

The C 1s XPS spectra for AG and NDG are shown in Fig. 1(a). The peak occurs at a binding energy of 284.6 eV for AG corresponding to sp^2 carbon [31]. For NDG the peaks are at 284.8, 285.8, and 288.5 eV corresponding to sp^2 carbon, C–N and C=O bonds [31]. The N 1s XPS spectra of NDG sample shown in Fig. 1(b) is fitted with two peaks corresponding to nongraphitic substitution, namely pyridinic (~399.5 eV) and pyrrolic (~400.5 eV) N [31,32]. In the pyridinic and pyrrolic structures the N atom bonds with two carbon atoms. We cannot resolve any quaternary (graphitic) substitution of N (generally occurs at a binding energy of ~401 eV). Raman spectra of the samples are recorded at room temperature using the excitation wavelength $\lambda = 514$ nm, displaying four bands [Fig. 1(c)] where peak positions and relative intensities are given in Table I. The G band is a symmetry allowed E_{2g} zone-center Γ point optical phonon and the D band is

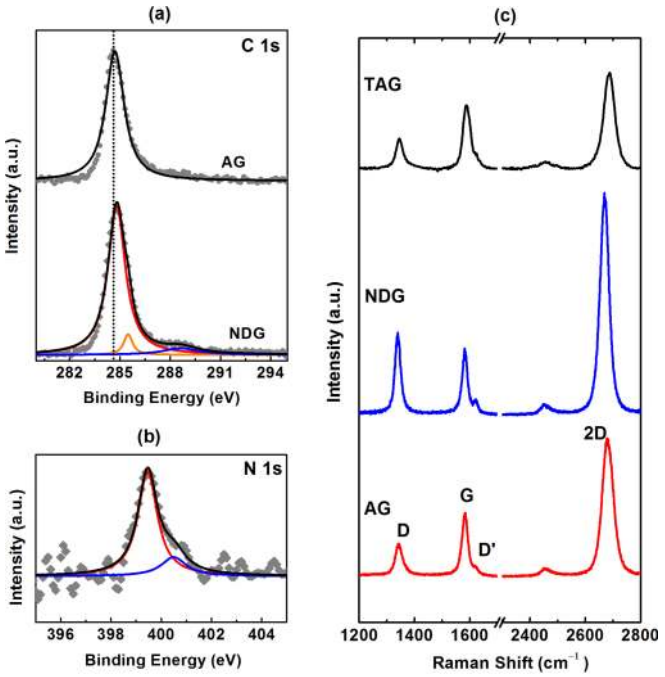

FIG. 1. (Color online) (a) XPS spectra of AG and NDG showing the C 1s line. The main peak at 284.6 eV represents sp^2 C. Two additional peaks appeared at 285.8 and 288.6 eV corresponding to C–N and C=O bonds. (b) The N 1s XPS spectra of NDG showing two peak at 399.5 and 400.5 eV, which suggest the presence of nongraphitic N–C bonding. (c) Raman spectra of AG, NDG, and TAG.

associated with the disorder activated near zone-boundary (K point) transverse optical phonon [33]. The $2D$ band is due to second-order Raman scattering from near K-point transverse optical phonons and is an unambiguous fingerprint of the number of layers, as understood by double resonance Raman scattering [33]. The D' band is associated with the disorder activated near Γ-point longitudinal optical phonons. The frequencies of the $2D$ and G bands and their relative intensities depend on the doping levels [34]. It is known that CVD grown graphene can be unintentionally p doped due to charge transfer from H_2O/O_2 molecules [35]. Using the intensity ratio of the $2D$ and G bands $I(2D)/I(G)$, the Fermi energy of the AG graphene is $E_F \sim -180$ meV [34]. After N doping the intensity ratio $I(2D)/I(G)$ increases which suggests [34] that the N doping has compensated the p doping in the AG shifting the Fermi level close to Dirac point with $E_F \sim -10$ meV. However, the exact value of E_F is difficult to estimate from the Raman data of NDG. The increase in the intensity of the D and D' bands after nitrogen doping clearly reveals an increase of the disorder in NDG. The ratio of the D and G band integrated intensities $A(D)/A(G)$ increase from ~0.6 in AG to ~1.3 in NDG. The ratio $A(D)/A(G)$ is empirically related [36] to the in-plane crystalline grain size without defects (L_a) as $A(D)/A(G) = [2.4 \times 10^{-10}\ \text{nm}^3]\lambda^4 L_a^{-1}$, which gives $L_a \sim 34$ nm for the AG, ~15 nm for the NDG, and ~38 nm for the TAG. Assuming the transport mean free path of the carriers $\ell \sim L_a$ and using Fermi velocity $v_F \approx 1 \times 10^6$ m/s [37], the average momentum relaxation time $\tau \sim \ell/v_F$ is ~15 fs in NDG, 34 fs in AG, and 38 fs in TAG. One may try to estimate the conductivity of the graphene in the strong scattering limit [16] by using $\sigma = G_0(E_F\tau/\hbar)$, giving $\sigma \sim 6G_0$ for AG, ~$1.4G_0$ for NDG, and ~$9G_0$ for TAG. The intensity ratio of D and D' bands $I(D)/I(D')$ has been related to the type of defects [38]. For the AG, $I(D)/I(D') \sim 7$ implies vacancylike defects, and $I(D)/I(D') \sim 8.7$ in NDG points to the presence of sp^3 defects as well [for sp^3 defects, $I(D)/I(D') \sim 13$] [38].

B. Terahertz conductivity of graphene

Let the temporal evolution of the transmitted terahertz electric fields through the graphene on the α-quartz substrate and through the substrate without graphene be denoted by $T_{\text{sam}}(t)$ and $T_{\text{ref}}(t)$, respectively. The ratio of Fourier transform (FT) of $T_{\text{sam}}(t)$ and $T_{\text{ref}}(t)$ gives amplitude and phase of the spectral transmission function $S(\omega) = \widetilde{T}_{\text{sam}}(\omega)/\widetilde{T}_{\text{ref}}(\omega)$. The complex conductivity spectra can be obtained from the spectral transmission function by using the relation $S(\omega) = [n_s + 1]/[n_s + 1 + Z_0\sigma]$ in the limit of thin film approximation [39,40]. Here $Z_0 = 377\ \Omega$ is the impedance of free space and n_s is the refractive index of substrate, taken as 2.2. Figure 2(a) shows the temporal terahertz fields through quartz (black line), AG (red line), and NDG (blue line). From the repeated runs, the error bar at the maximum of the THz electric field is estimated to be ~8%. The inset shows the signal on an expanded scale near the maximum of the electric field. It can be seen that for NDG, the obtained difference in the peak value of the electric field is ~14%, barely above the uncertainty level of the measurements. Figure 2(b) shows the real part of the conductivity in the spectral range 0.5 to 2.5 THz and the corresponding FTs are shown in the inset. A nearly spectrally flat conductivity suggests large momentum scattering rate for the graphene samples, i.e., $\omega\tau \ll 1$ [11,19,41], as also suggested by the estimates of τ from the Raman data (see Table I). The average conductivities of AG, NDG, and TAG samples are $(7 \pm 1)G_0$, $(1.0 \pm 0.5)G_0$, and $(4 \pm 1)G_0$, respectively, in close agreement with the estimates obtained from the Raman data. For the NDG sample, the value of the average conductivity is only approximate. The reduction of conductivity of the NDG is due to the shift of the Fermi level towards the Dirac point and a decrease of the momentum relaxation time due to increase in disorder.

TABLE I. Raman characterization.

Sample	G (cm^{-1})	$I(2D)/I(G)$	$A(D)/A(G)$	$I(D)/I(D')$	Fermi energy, E_F (meV)	Crystalline size, L_a (nm)
AG	1583	2.4	0.6	7.0	−180	34
NDG	1582	3.5	1.3	8.7	−10	15
TAG	1589	1.5	0.5	5.7	−200	38

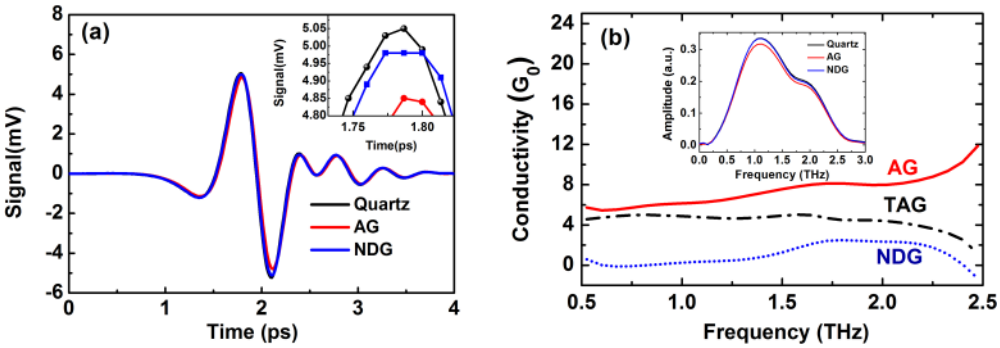

FIG. 2. (Color online) Terahertz conductivity. (a) Evolution of THz electric field as a function of delay time. (b) Conductivity (in unit of G_0) spectra for AG (red solid line), NDG (blue dotted line), and TAG (black dash-dotted line). Inset: FT amplitudes vs frequency.

C. Optical-pump induced changes in terahertz conductivities

The differential transmission $\Delta T/T$ is related to the dynamic THz conductivity $\Delta\sigma$ by the relation $\frac{\Delta T}{T} \approx -\frac{Z_0}{n_s+1}\Delta\sigma$. The results shown in Fig. 3 corresponds to the peak of the THz electric field using a pump excitation density of 340 μJ/cm^2 per pulse. Taking the absorption at 785 nm to be 2.3%, photoexcited carrier density is 3×10^{13}/cm^2 [42]. Most interestingly, $\Delta\sigma$ is negative for the AG, whereas it is positive for the NDG. After annealing the NDG, $\Delta\sigma$ is once again negative for TAG.

To understand our results, we now analyze various contributions to the dynamic conductivity. As mentioned earlier, hot carriers achieve quasiequilibrium Fermi distribution with electron temperature T_e, thus $\Delta\sigma = \sigma(T_e) - \sigma(T_0)$, where T_0 is the lattice temperature (=300 K). The intraband and interband contributions to dynamic conductivity is calculated using [43]

$$\sigma_{\text{intra}}(T) = \frac{2G_0\tau k_B T}{\hbar(\omega^2\tau^2+1)}\left[2\cosh\left(-\frac{E_F}{2k_BT}\right)\right], \quad (1)$$

$$\sigma_{\text{inter}}(T) = \frac{\pi G_0}{8}\left[\tanh\left(\frac{\hbar\omega+2E_F}{4k_BT}\right)+\tanh\left(\frac{\hbar\omega-2E_F}{4k_BT}\right)\right], \quad (2)$$

where ω is the terahertz-probe frequency. The interband contribution (see Supplemental Material [44], Fig. s1) gives positive and negative $\Delta\sigma$ depending on E_F but is $\sim 10^3$ times smaller as compared to the intraband contribution for any finite E_F. Hence the photoinduced terahertz conductivity is dominated by the intraband scattering [11,19,43] and henceforth we will neglect interband contributions. Taking $\tau = 34$ fs, the intraband contribution to the dynamic conductivity at 1 THz is shown in Fig. 4(a) (dotted black line) as a function of Fermi energy at a representative $T_e = 700$ K. In this estimation we have taken into account the change in Fermi energy of graphene as a function of electronic temperature for a fixed carrier concentration. The magnitude of $\Delta\sigma_{\text{intra}}$ as seen in Fig. 4(a) is not sufficient to explain the observed $\Delta\sigma$ in AG ($E_F \sim -180$ meV), which necessarily requires another mechanism.

We consider the recently proposed secondary hot carrier generation (SHCG) [16] in which the photoexcited carriers interact with the intrinsic carriers to excite the later. The photoexcited carriers have two scattering channels; one is the conventional intraband scattering mechanism with momentum relaxation time τ, as discussed earlier, and the other is the Coulomb scattering with momentum relaxation time τ_e, which is proportional to carrier energy ε, i.e., $\tau_e = b\varepsilon$. Here b, the proportionality constant, depends on the ratio of the average interelectron Coulomb interaction energy to the Fermi energy and the density of the secondary hot carriers (n_i) (see Eq. (3.21) of Ref. [45]). The secondary hot carrier generation contribution to the photoinduced conductivity is given by [16]

$$\Delta\sigma_{\text{el}} = k_B^2\left(T_e^2 - T_0^2\right)\frac{\pi^2}{6}\nu(E_F)\left.\frac{\partial^2 F(\varepsilon)}{\partial\varepsilon^2}\right|_{\varepsilon=E_F}, \quad (3)$$

$$F(\varepsilon) = e^2 v_F^2 \frac{\tau_e(\varepsilon)}{1+\omega^2[\tau_e(\varepsilon)]^2}, \quad (4)$$

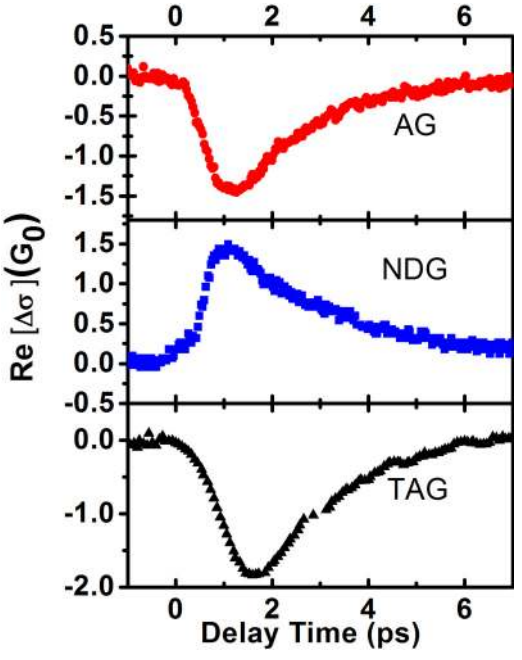

FIG. 3. (Color online) Transient THz photoconductivity. Evolution of the real part of photoinduced THz conductivity as function of delay time between the 785 nm pump and the THz probe.

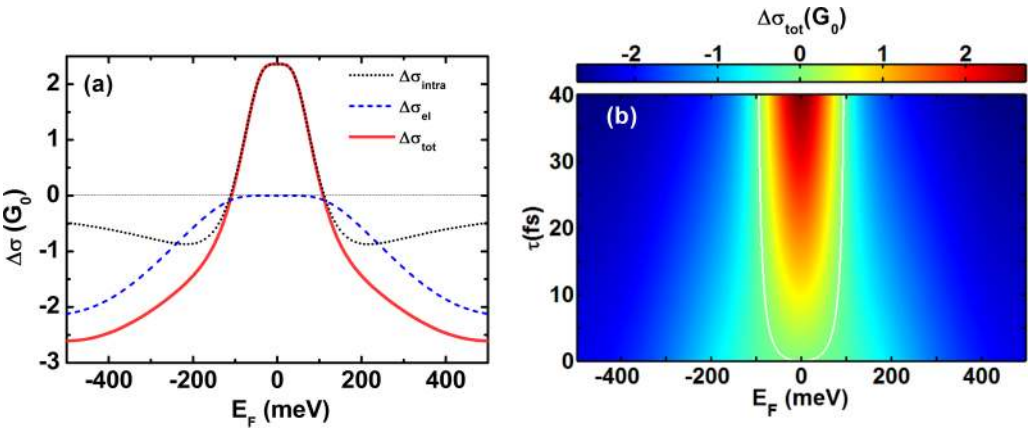

FIG. 4. (Color online) Scattering mechanisms. (a) $\Delta\sigma_{\text{intra}}$, $\Delta\sigma_{\text{el}}$, and $\Delta\sigma_{\text{tot}}$ are plotted as a function of Fermi energy E_F at $T_e = 700$ K, $\tau = 34$ fs, and $b = 190$ fs/eV for probe frequency $\omega/2\pi = 1$ THz. (b) The contour plot of $\Delta\sigma_{\text{tot}}$ as a function of Fermi energy and momentum relaxation time τ at $T_e = 700$ K and $b = 190$ fs/eV. The white line represents $\Delta\sigma_{\text{tot}} = 0$ and indicates the boundary between positive and negative $\Delta\sigma_{\text{tot}}$.

where $\nu(E_F)$ is density of states of graphene at Fermi energy. As suggested in Ref. [16], we estimate $b = 190$ fs/eV after taking $\tau_e = 34$ fs and $E_F = -180$ meV in calculating $\Delta\sigma_{\text{el}}$. Figure 4(a) (dashed blue line) shows that $\Delta\sigma_{\text{el}} < 0$ and the magnitude is comparable to the intraband contribution to the terahertz dynamic conductivity. The total change of terahertz photoconductivity is the sum of intraband and the SHCG contributions: $\Delta\sigma_{\text{tot}} = \Delta\sigma_{\text{intra}} + \Delta\sigma_{\text{inter}}$. Figure 4(b) shows the dynamic terahertz photoconductivity at 1 THz as a function of Fermi energy E_F and momentum relaxation time τ at a representative electron temperature of 700 K. It shows that the magnitude and sign of $\Delta\sigma_{\text{tot}}$ is determined by the value of the Fermi energy and the momentum relaxation time. In AG, $E_F \sim -180$ meV and $\tau \sim 34$ fs gives negative $\Delta\sigma_{\text{tot}}$, whereas a shift of Fermi level towards the Dirac point in NDG results in $\Delta\sigma_{\text{tot}} > 0$ due to dominance of the intraband scattering process. Again, in TAG the increased Fermi energy lead to $\Delta\sigma_{\text{tot}} < 0$. The results are similar for other representative values of parameter b ($b = 120$, 300 fs/eV) [44].

The dependence of THz photoconductivity on laser fluence is studied in term of electron temperature. Immediately after pump excitation the sharp change of the THz conductivity is due to the heating of carriers followed by quasiequilibrium carrier distribution with electron temperature $T_e(0)$. Here $T_e(0)$ corresponds to maximum of $|\Delta\sigma|$. One can extract $T_e(0)$ from $|\Delta\sigma|^{\max}$ by using Eqs. (1) and (3). Figure 5 shows the fluence dependence of increase in electron temperature $\Delta T_e(0)$ $[= T_e(0) - T_0]$ at the peak of transient conductivity. It is clear that $\Delta T_e(0)$ is a sublinear function of fluence and is best described by $\varphi^{1/3}$, as shown by solid lines in Fig. 5. This is expected in graphene due to its linear electronic band dispersion [13,46]. However, a few recent works have reported $\varphi^{1/2}$ behavior in very highly doped graphene ($E_F > 260$ meV) [17,27]. Since the electron heat capacity of graphene is proportional to the density of state and hence the Fermi energy [27,47], the NDG will have smaller electronic heat capacity than that of AG and therefore the electron temperature T_e in NDG will be more than that in AG for a given pump fluence. This is indeed the case as seen in Fig. 5: $\Delta T_e(0) = (380 \pm 34)$ K in AG and $\Delta T_e(0) = (555 \pm 50)$ K in NDG at $\varphi = 340\ \mu\text{J/cm}^2$.

D. Cooling dynamics

We now focus on the cooling dynamics of the photoexcited carriers. As mentioned before, due to strong electron phonon coupling the hot carriers can efficiently lose their energy by optical phonon emission within 100–500 fs till their energy comes down to 200 meV. Below 200 meV, the hot carriers can dissipate energy only by emitting acoustic phonons with energy $k_B T_{\text{BG}}$ per scattering event as permitted by conservation of momentum. Here T_{BG} is a Bloch-Grüneisen temperature given by $k_B T_{\text{BG}} = (2v_s/v_F)E_F$ ($v_s \sim 2.1 \times 10^4$ m/s is velocity of sound in graphene) which defines a boundary between the low and the high temperature behavior. The cooling of carriers can

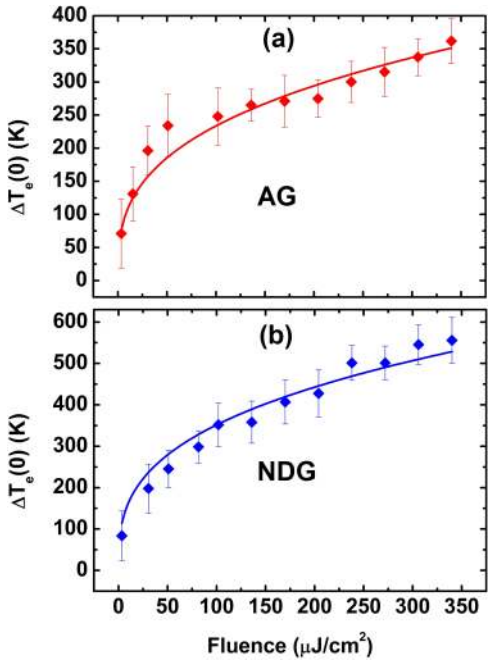

FIG. 5. (Color online) The photoinduced change of electron temperature $\Delta T_e(0)$ at the peak of transient conductivity is plotted as a function of fluence for (a) AG and (b) NDG. The solid lines are the fit to $\varphi^{1/3}$.

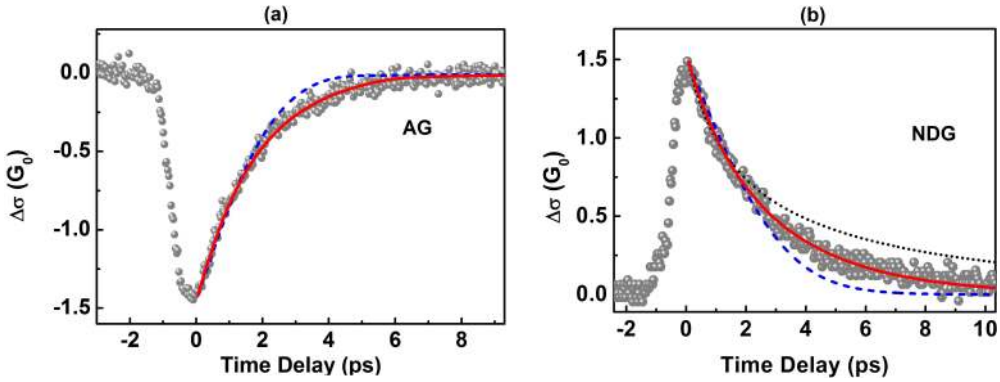

FIG. 6. (Color online) (a) Cooling dynamics of AG. The blue dashed line is fit to normal collision given by Eq. (5) and red solid line is fit to SC given by Eq. (6). (b) Cooling dynamics of NDG. The black dotted curve is fit to normal collision in the nondegenerate limit [Eq. (8)], the blue dashed curve is fit to normal collision in degenerate limit [Eq. (5)], and the red solid curve is fit to SC given by Eq. (6).

last tens of picoseconds for phonon temperature $T_0 > T_{BG}$. However, in the presence of disorder an alternate route of energy relaxation is via disorder-mediated emission of high energy ($\sim k_B T_e$) and high momentum ($\sim k_B T_e/\hbar v_s$) acoustic phonons, named as supercollision (SC) cooling. With this background we can evaluate different mechanisms to identify the cooling dynamics. The cooling laws are given by [47,48]

$$\frac{\partial T_e(t)}{\partial t} = B\frac{(T_e - T_0)}{T_e}, \quad \text{for normal collisions} \tag{5}$$

$$= A\frac{\left(T_e^3 - T_0^3\right)}{T_e}, \quad \text{for SC} \tag{6}$$

in the degenerate limit. $B = 3D_{ac}^2 E_F^3/4\pi^2\rho v_F^4\hbar^3 k_B$ is the normal cooling rate coefficient and $A = 6\zeta(3)gk_B/\pi^2 k_F \ell\hbar$ is the SC cooling rate coefficient. Here D_{ac} is the deformation potential, $\rho \sim 7.6 \times 10^{-7}\,\mathrm{kg/m^2}$, ζ is the Riemann zeta function, and g is the electron-phonon coupling strength given by $g = 2D_{ac}^2 E_F/\rho v_s^2 \pi(\hbar v_F)^2$.

The enhancement factor for energy dissipation rate over momentum conserving path ways is expressed as [47]

$$\frac{H_{SC}}{H_0} = \frac{0.77}{k_F\ell}\frac{T_e^2 + T_e T_0 + T_0^2}{T_{BG}^2}. \tag{7}$$

Therefore, the enhancement factor depends on temperature, Fermi energy, and disorder. The temperature T_{BG} is ~87 K for AG and ~5 K for NDG which are less than T_0 (=300 K). The enhancement factor from Eq. (7) is ~17 380 for NDG and ~13 for AG, taking $T_e = 700$ K and $T_0 = 300$ K, clearly showing the dominance of the SC cooling. To further make sure whether SC cooling is the dominant mechanism or not, we fit the dynamic conductivity $\Delta\sigma(t)$ shown in Figs. 6(a) and 6(b),F6 taking into account both normal collisions [Eq. (5)] as well as supercollision [Eq. (6)] together with Eqs. (1), (3), and (4). The blue dashed curve in Fig. 6(a) shows the best fitting to normal collision model with $B = 3 \times 10^{14}\,\mathrm{K\,s^{-1}}$. This value of B gives very unreasonable high deformation potential $D_{ac} = 260$ eV. In comparison, the red solid line in Fig. 6(a) shows the best fitting to the SC with $A = 5.0 \times 10^8\,\mathrm{K^{-1}\,s^{-1}}$ in AG. This value of A gives $D_{ac} = 17$ eV, a reasonable value in agreement with reported values [49,50]. Here we have used $k_F\ell = \sigma(h/2e^2) \sim 6$, $|E_F| = 180$ meV, and $\tau = 34$ fs. This exercise tells us that the SC model explains our data for the AG sample better than the normal collision model.

Coming to NDG [Fig. 6(b)], since E_F is close to the Dirac point, we consider the normal collisions in the nondegenerate limit ($E_F \ll k_B T_e$) where the cooling law for acoustic phonon emission is given by [48]

$$\frac{\partial T_e(t)}{\partial t} = CT_e^2(T_e - T_0). \tag{8}$$

The dotted line in Fig. 6(b) shows the best fitted curve [Eq. (8)] with $C = 7.6 \times 10^5\,(\mathrm{K^2 s})^{-1}$, which not only reveals poor fitting but also gives a unphysical value of the deformation potential $D_{ac} = 293$ eV. Next we test if it is possible to fit the data by normal collision model [Eq. (5)]. Here again, the dashed blue curve in Fig. 6(b) shows poor fitting for normal collision with an unreasonable value of $D_{ac} = 1.95 \times 10^4$ eV. The best fitting is obtained by using the SC model [Eq. (6)] with $A = 3.6 \times 10^8\,\mathrm{K^{-1}\,s^{-1}}$, as shown by the solid red line. The extracted D_{ac} is ~28 eV comparable to the known values [49,50]. Here we have used $|E_F| = 10$ meV and $k_F\ell = \sigma(h/2e^2) \sim 1.4$ to extract the deformation potential. Though it is clear that SC cooling dynamics can explain the data very nicely, the confirmation of SC decay law would require lattice temperature dependent cooling measurements that are beyond the scope of this work.

E. Frequency dependence of dynamic conductivity

We now present the frequency dependence of the dynamic conductivity. After the pump excitation, the photoinduced change in terahertz electric field $\Delta T(t)$ throughout the complete terahertz pulse is measured [44] for a pump fluence of ~340 $\mu\mathrm{J/cm^2}$ and Figs. 7(a)–7(c) show the real and imaginary parts of photoinduced conductivity for AG, NDG, and TAG, respectively. In AG the zero crossing of the imaginary part of $\Delta\sigma$ at 1.3 THz clearly suggests a corresponding peak in the real part of $\Delta\sigma$ which can be described by a Lorentzian oscillator. However, the amplitude of the imaginary part is much less than the real part and points to the Drude behavior. Hence the Drude-Lorentz model has been used to describe the

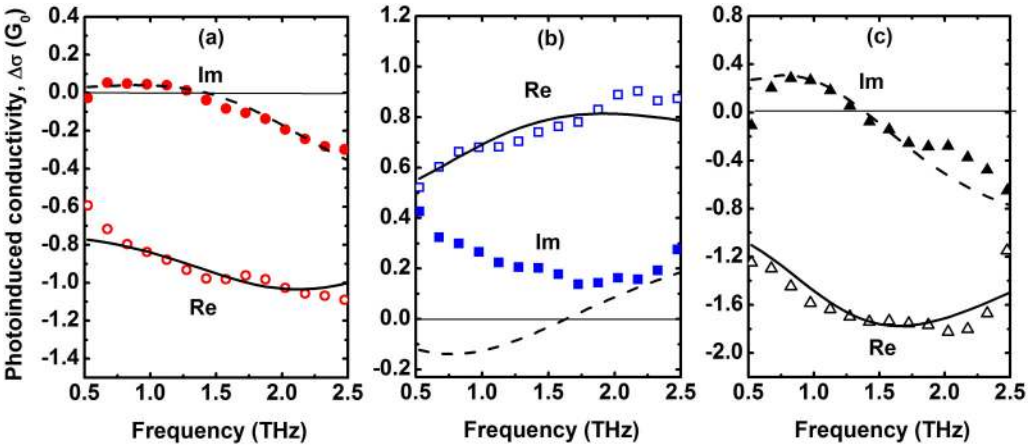

FIG. 7. (Color online) Photoinduced conductivity $\Delta\sigma(\omega)$ as a function of frequency at 2 ps after photoexcitation for (a) AG, (b) NDG, and (c) TAG. The real parts of the data are shown by opened symbols and imaginary parts are shown by closed symbols. The continuous horizontal lines shows the zero reference lines of $\Delta\sigma(\omega)$. The black and dashed nonlinear black lines are the fit to the Drude-Lorentz model [Eq. (9)].

frequency dependence of $\Delta\sigma(\omega)$ [20,51,52]:

$$\Delta\sigma(\omega) = \frac{\mathfrak{D}\tau}{1 - i\omega\tau} + \frac{iF\omega}{(\omega^2 - \omega_0^2) + i\omega\gamma}. \qquad (9)$$

Here the first term is the Drude part in terms of Drude weight $\mathfrak{D}$ and momentum relaxation time τ. The second term is the Lorentz part with F as the oscillator strength, γ as linewidth, and ω_0 as the resonant frequency. The fitted curves are shown in Fig. 7(a) for the AG ($\mathfrak{D} = 1.7 \times 10^9\ \Omega^{-1}\,\mathrm{s}^{-1}$, $\tau = 34$ fs, $F = 5.9 \times 10^8\ \Omega^{-1}\,\mathrm{s}^{-1}$, $\gamma = 18$ THz, $\omega_0/2\pi = 2.3$ THz). In comparison, for the NDG the imaginary part is positive as in the Drude-like response but the positive real part shown in Fig. 7(b) cannot be explained by the Drude model. The Drude-Lorentz model [Eq. (9)] is not able to fit the imaginary part of $\Delta\sigma(\omega)$ [Fig. 7(b)], a discrepancy which needs to be understood further. Here we have used $\tau = 15$ fs (obtained from Raman scattering) and $\omega_0/2\pi = 2.0$ THz. The $\Delta\sigma(\omega)$ of TAG is nearly same as that of the AG and fitted with the Drude-Lorentz model with $\mathfrak{D} = 1.8 \times 10^9\ \Omega^{-1}\,\mathrm{s}^{-1}$, $\tau = 38$ fs, $F = 1.5 \times 10^9\ \Omega^{-1}\,\mathrm{s}^{-1}$, $\gamma = 19$ THz, and $\omega_0/2\pi = 1.7$ THz, as shown in Fig. 7(c).

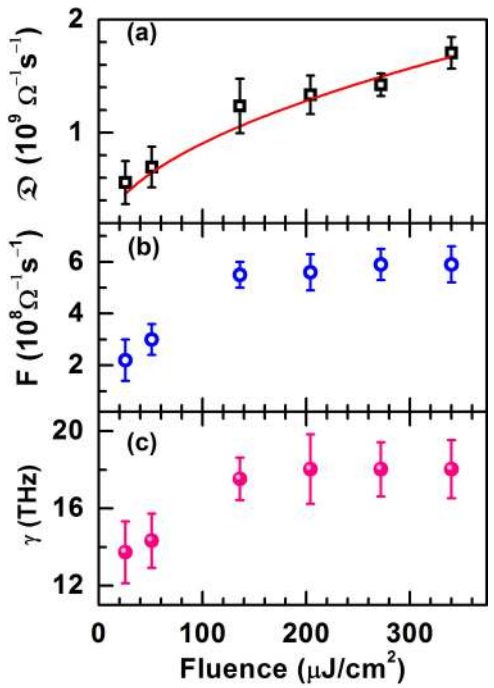

FIG. 8. (Color online) Fitted parameters for AG. (a) The Drude weight $\mathfrak{D}$ varies as $\varphi^{1/2}$ (shown by the red solid line). (b) and (c) Oscillator strength F and linewidth γ as a function of pump fluence.

The dynamic conductivity $\Delta\sigma(\omega)$ of the AG was measured as a function of pump fluence varying from 25 to 340 μJ/cm^2 [44]. The best fit of the Drude-Lorentz model is obtained by taking $\tau = 34$ fs and $\omega_0/2\pi = 2.3$ THz and varying $\mathfrak{D}$, F, and γ. The fluence dependence of these parameters are shown in Figs. 8(a)–8(c). It is seen that $\mathfrak{D} \sim \varphi^{1/2}$ [see the solid line in Fig. 8(a)], as expected for graphene [$\mathfrak{D} = (v_F e^2/\hbar)\sqrt{\pi\Delta n}$], where Δn is the density of photoinduced carriers participating in intraband scattering.

The physical significance of the resonant frequency ω_0 in Lorentz part of $\Delta\sigma$ is not clear. Docherty *et al.* [20] have considered two possible explanations: excitation of plasmon and a band gap opening. The first possibility in our case is ruled out since ω_0 is seen to be fluence independent, similar to Docherty *et al.* The second explanation in terms of band gap opening of ~9.4 meV, equivalent to $\omega_0/2\pi = 2.3$ THz, seems to be possible, specially in the light of recent work which shows that a band gap can open in graphene due to laser-induced two photon oxidation [53].

IV. CONCLUSION

In summary, we have presented a quantitative framework of THz dynamic conductivity in monolayer graphene. We showed that $\Delta\sigma$ is determined by the relative contributions of the secondary hot carrier generation and conventional intraband scattering which, in turn, depend on the position of the Fermi level and momentum relaxation time. In a highly doped sample, the photoexcited hot electrons interact with the intrinsic carriers to generate secondary hot carriers which result in a decrease of the THz conductivity. In NDG, the Fermi

energy is closer to the Dirac point and the enhanced disorder decreases the momentum relaxation time which makes the intraband scattering as the dominant scattering mechanism resulting in positive $\Delta\sigma$. The cooling dynamics of the hot carriers is well explained in both samples by the disorder-mediated electron-acoustic phonon interaction, giving the deformation potential comparable to the previous studies. It will be worthwhile to further do OPTP measurements as a function of lattice temperature to further understand the cooling dynamics.

ACKNOWLEDGMENTS

A.K.S. thanks the Nano Mission Project under the Department of Science and Technology, Government of India for funding. We thank Gyan Prakash for his help in the initial part of the experiments.

[1] F. Bonaccorso, Z. Sun, T. Hasan, and A. C. Ferrari, Nat. Photon. **4**, 611 (2010).
[2] K. S. Novoselov, A. K. Geim, S. V. Morozov, D. Jiang, M. I. Katsnelson, I. V. Grigorieva, S. V. Dubonos, and A. A. Firsov, Nature (London) **438**, 197 (2005).
[3] S. V. Morozov, K. S. Novoselov, M. I. Katsnelson, F. Schedin, D. C. Elias, J. A. Jaszczak, and A. K. Geim, Phys. Rev. Lett. **100**, 016602 (2008).
[4] P. Avouris, Nano Lett. **10**, 4285 (2010).
[5] A. K. Geim and K. S. Novoselov, Nat. Mater. **6**, 183 (2007).
[6] P. Weis, J. L. Garcia-Pomar, M. Höh, B. Reinhard, A. Brodyanski, and M. Rahm, ACS Nano **6**, 9118 (2012).
[7] Q. Bao and K. P. Loh, ACS Nano **6**, 3677 (2012).
[8] H. Wang, J. H. Strait, P. A. George, S. Shivaraman, V. B. Shields, M. Chandrashekhar, J. Hwang, F. Rana, M. G. Spencer, C. S. Ruiz-Vargas, and J. Park, Appl. Phys. Lett. **96**, 081917 (2010).
[9] H. Choi, F. Borondics, D. A. Siegel, S. Y. Zhou, M. C. Martin, A. Lanzara, and R. A. Kaindl, Appl. Phys. Lett. **94**, 172102 (2009).
[10] J. M. Dawlaty, S. Shivaraman, M. Chandrashekhar, F. Rana, and M. G. Spencer, Appl. Phys. Lett. **92**, 042116 (2008).
[11] P. A. George, J. Strait, J. Dawlaty, S. Shivaraman, M. Chandrashekhar, F. Rana, and M. G. Spencer, Nano Lett. **8**, 4248 (2008).
[12] D. Sun, C. Divin, C. Berger, W. A. de Heer, P. N. First, and T. B. Norris, Phys. Rev. Lett. **104**, 136802 (2010).
[13] I. Gierz, J. C. Petersen, M. Mitrano, C. Cacho, I. C. E. Turcu, E. Springate, A. Stöhr, A. Köhler, U. Starke, and A. Cavalleri, Nat. Mater. **12**, 1119 (2013).
[14] J. C. W. Song, K. J. Tielrooij, F. H. L. Koppens, and L. S. Levitov, Phys. Rev. B **87**, 155429 (2013).
[15] J. C. W. Song, M. S. Rudner, C. M. Marcus, and L. S. Levitov, Nano Lett. **11**, 4688 (2011).
[16] K. J. Tielrooij, J. C. W. Song, S. A. Jensen, A. Centeno, A. Pesquera, A. Zurutuza Elorza, M. Bonn, L. S. Levitov, and F. H. L. Koppens, Nat. Phys. **9**, 248 (2013).
[17] M. W. Graham, S.-F. Shi, D. C. Ralph, J. Park, and P. L. McEuen, Nat. Phys. **9**, 103 (2013).
[18] C. J. Divin, D. Sun, C. Berger, W. de Heer, P. N. First, and T. B. Norris, *Conference on Lasers and Electro-Optics/International Quantum Electronics Conference* (Optical Society of America, Washington, DC, 2009), p. CMT2.
[19] J. H. Strait, H. Wang, S. Shivaraman, V. Shields, M. Spencer, and F. Rana, Nano Lett. **11**, 4902 (2011).
[20] C. J. Docherty, C.-T. Lin, H. J. Joyce, R. J. Nicholas, L. M. Herz, L.-J. Li, and M. B. Johnston, Nat. Commun. **3**, 1228 (2012).
[21] G. Jnawali, Y. Rao, H. Yan, and T. F. Heinz, Nano Lett. **13**, 524 (2013).
[22] A. J. Frenzel, C. H. Lui, W. Fang, N. L. Nair, P. K. Herring, P. Jarillo-Herrero, J. Kong, and N. Gedik, Appl. Phys. Lett. **102**, 113111 (2013).
[23] H. Karasawa, T. Komori, T. Watanabe, A. Satou, H. Fukidome, M. Suemitsu, V. Ryzhii, and T. Otsuji, J. Infrared Millimeter Terahertz Waves **32**, 655 (2011).
[24] V. Ryzhii, M. Ryzhii, and T. Otsuji, J. Appl. Phys. **101**, 083114 (2007).
[25] A. Satou, V. Ryzhii, Y. Kurita, and T. Otsuji, J. Appl. Phys. **113**, 143108 (2013).
[26] T. Otsuji, S. Boubanga-Tombet, A. Satou, M. Suemitsu, and V. Ryzhii, J. Infrared Millimeter Terahertz Waves **33**, 825 (2012).
[27] S.-F. Shi, T.-T. Tang, B. Zeng, L. Ju, Q. Zhou, A. Zettl, and F. Wang, Nano Lett. **14**, 1578 (2014).
[28] X. Li, W. Cai, J. An, S. Kim, J. Nah, D. Yang, R. Piner, A. Velamakanni, I. Jung, E. Tutuc, S. K. Banerjee, L. Colombo, and R. S. Ruoff, Science **324**, 1312 (2009).
[29] R. Lv, Q. Li, A. R. Botello-Mndez, T. Hayashi, B. Wang, A. Berkdemir, Q. Hao, A. L. Elas, R. Cruz-Silva, H. R. Gutirrez, Y. A. Kim, H. Muramatsu, J. Zhu, M. Endo, H. Terrones, J.-C. Charlier, M. Pan, and M. Terrones, Sci. Rep. **2**, 586 (2012).
[30] J. W. Suk, A. Kitt, C. W. Magnuson, Y. Hao, S. Ahmed, J. An, A. K. Swan, B. B. Goldberg, and R. S. Ruoff, ACS Nano **5**, 6916 (2011).
[31] Y. Wang, Y. Shao, D. W. Matson, J. Li, and Y. Lin, ACS Nano **4**, 1790 (2010).
[32] H. Gao, L. Song, W. Guo, L. Huang, D. Yang, F. Wang, Y. Zuo, X. Fan, Z. Liu, W. Gao, R. Vajtai, K. Hackenberg, and P. M. Ajayan, Carbon **50**, 4476 (2012).
[33] L. Malard, M. Pimenta, G. Dresselhaus, and M. Dresselhaus, Phys. Rep. **473**, 51 (2009).
[34] A. Das, S. Pisana, B. Chakraborty, S. Piscanec, S. K. Saha, U. V. Waghmare, K. S. Novoselov, H. R. Krishnamurthy, A. K. Geim, A. C. Ferrari, and A. K. Sood, Nat. Nano. **3**, 210 (2008).
[35] D.-W. Shin, H. M. Lee, S. M. Yu, K.-S. Lim, J. H. Jung, M.-K. Kim, S.-W. Kim, J.-H. Han, R. S. Ruoff, and J.-B. Yoo, ACS Nano **6**, 7781 (2012).
[36] L. G. Canado, K. Takai, T. Enoki, M. Endo, Y. A. Kim, H. Mizusaki, A. Jorio, L. N. Coelho, R. Magalhes-Paniago, and M. A. Pimenta, Appl. Phys. Lett. **88**, 163106 (2006).
[37] A. H. Castro Neto, F. Guinea, N. M. R. Peres, K. S. Novoselov, and A. K. Geim, Rev. Mod. Phys. **81**, 109 (2009).
[38] A. Eckmann, A. Felten, A. Mishchenko, L. Britnell, R. Krupke, K. S. Novoselov, and C. Casiraghi, Nano Lett. **12**, 3925 (2012).
[39] J. L. Tomaino, A. D. Jameson, J. W. Kevek, M. J. Paul, A. M. van der Zande, R. A. Barton, P. L. McEuen, E. D. Minot, and Y.-S. Lee, Opt. Express **19**, 141 (2011).
[40] M. Tinkham, Phys. Rev. **104**, 845 (1956).

[41] W. Liu, R. Valds Aguilar, Y. Hao, R. S. Ruoff, and N. P. Armitage, J. Appl. Phys. **110**, 083510 (2011).

[42] K. F. Mak, M. Y. Sfeir, Y. Wu, C. H. Lui, J. A. Misewich, and T. F. Heinz, Phys. Rev. Lett. **101**, 196405 (2008).

[43] S. Winnerl, M. Orlita, P. Plochocka, P. Kossacki, M. Potemski, T. Winzer, E. Malic, A. Knorr, M. Sprinkle, C. Berger, W. A. de Heer, H. Schneider, and M. Helm, Phys. Rev. Lett. **107**, 237401 (2011).

[44] See Supplemental Material at http://link.aps.org/supplemental/10.1103/PhysRevB.90.165420 for interband conductivity shown in Fig. s1, contour plot of $\Delta\sigma_{\text{tot}}$ shown in Fig. s2, the temporal evolution of photoinduced THz pulse shown in Fig. s3, and spectral dependence of photoinduced complex conductivity of AG at different pump fluences shown in Fig. s4.

[45] S. Das Sarma, S. Adam, E. H. Hwang, and E. Rossi, Rev. Mod. Phys. **83**, 407 (2011).

[46] T. Winzer and E. Malić, Phys. Rev. B **85**, 241404 (2012).

[47] J. C. W. Song, M. Y. Reizer, and L. S. Levitov, Phys. Rev. Lett. **109**, 106602 (2012).

[48] R. Bistritzer and A. H. MacDonald, Phys. Rev. Lett. **102**, 206410 (2009).

[49] K. I. Bolotin, K. J. Sikes, J. Hone, H. L. Stormer, and P. Kim, Phys. Rev. Lett. **101**, 096802 (2008).

[50] C. R. Dean, A. F. Young, I. Meric, C. Lee, L. Wang, S. Sorgenfrei, K. Watanabe, T. Taniguchi, P. Kim, K. L. Shepard, and J. Hone, Nat. Nano. **5**, 722 (2010).

[51] P. Parkinson, J. Lloyd-Hughes, Q. Gao, H. H. Tan, C. Jagadish, M. B. Johnston, and L. M. Herz, Nano Lett. **7**, 2162 (2007).

[52] P. Parkinson, H. J. Joyce, Q. Gao, H. H. Tan, X. Zhang, J. Zou, C. Jagadish, L. M. Herz, and M. B. Johnston, Nano Lett. **9**, 3349 (2009).

[53] J. Aumanen, A. Johansson, J. Koivistoinen, P. Myllyperkiö, and M. Pettersson, arXiv:1408.0905.